Nature 516.7531 (2014): 374-378

DOI: http://dx.doi.org/10.1038/nature14026

Reconstruction and Control of a Time-Dependent Two-Electron Wave Packet

Christian Ott[1,2], Andreas Kaldun[1], Luca Argenti[3], Philipp Raith[1], Kristina Meyer[1], Martin Laux[1], Yizhu Zhang[1], Alexander Blättermann[1], Steffen Hagstotz[1], Thomas Ding[1], Robert Heck[1], Javier Madroñero[4], Fernando Martín[3,5], and Thomas Pfeifer[1,6]

[1]Max-Planck Institut für Kernphysik, Saupfercheckweg 1, 69117 Heidelberg, Germany
[2]Present Address: Chemistry Department, University of California, Berkeley, California, 94720, USA
[3]Departamento de Química, Módulo 13, Universidad Autónoma de Madrid, 28049 Madrid, Spain
[4]Physik Department, TU München, 85747 Garching
[5]Instituto Madrileño de Estudios Avanzados en Nanociencia (IMDEA-Nano), Cantoblanco, 28049 Madrid, Spain
[6]Center for Quantum Dynamics, Ruprecht-Karls-Universität Heidelberg, 69120 Heidelberg, Germany

The concerted motion of two or more bound electrons governs atomic[1] and molecular[2,3] non-equilibrium processes and chemical reactions. It is thus a long-standing scientific dream to measure and control the dynamics of two bound and correlated electrons in the quantum regime. At least two active electrons and a nucleus are required to address such quantum three-body problem[4] for which analytical solutions do not exist, a condition that is met in the helium atom. While attosecond dynamics were previously observed for single-active electron/hole cases[5-7], such time-resolved observation of two-electron motion thus far remained an unaccomplished challenge. Here, we measure a 1.2-femtosecond quantum beat among low-lying doubly-excited states in helium and use it to reconstruct a correlated two-electron wave packet. Our experimental method combines attosecond transient-absorption spectroscopy[5,7-9] at unprecedented high spectral resolution (20 meV s.d. near 60 eV) with an intensity-tuneable visible laser field to couple[10-12] the quantum states from the weak-field to the strong-coupling regime. Employing the Fano resonance as a phase-sensitive quantum interferometer[13], we demonstrate the coherent control of two correlated electrons, which form the basis of most covalent molecular bonds in nature. As we show, such multi-dimensional spectroscopy experiments provide benchmark data for testing fundamental few-body quantum-dynamics theory. They also light a route for site-specific measurement and control of metastable electronic transition states that are at the heart of fundamental reactions in chemistry and biology.

Electrons are bound to atoms and molecules by the Coulomb force of the nuclei. Moving between atoms, they form the basis of the molecular bond. The same Coulomb force, however, acts repulsively between the electrons. This electron–electron interaction represents a major challenge in the understanding and modelling of atomic and molecular states, their structure and in particular their dynamics[2,3,14]. Here, we focus on the ^{1}P $sp_{2,n+}$ series[15] of doubly-excited states in helium below the $N = 2$ ionization threshold. They are excited by a single-photon transition from the ^{1}S $1s^2$ ground state by the promotion of both electrons to at least principal quantum number $n = 2$. The states autoionize due to electron–electron interaction and their spectroscopic signature manifests as asymmetric non-Lorentzian line shapes. The latter were first observed in the 1930s[16] and attributed[17], by Ugo Fano, to the quantum interference of bound states with the continuum to which they are coupled (Fig. 1c,d). The coupling is described by the configuration

interaction V_{CI} with the single-ionization continuum $|1s,\varepsilon p\rangle$, where one electron is in the 1s ground state and the other one is in the continuum with kinetic energy ε. The magnitude of V_{CI} determines the lifetimes of the transiently bound states. In our case, these range between 17 fs for the 2s2p ($sp_{2,2}$)[18] and several hundreds of femtoseconds for some higher-lying $sp_{2,n+}$ states[15]. As these lifetimes are that short, with energy-level spacings on the order of several eV, the coupling dynamics between the states in external fields must be measured using ultrashort pulses. Previous time-resolved experiments observed the light-induced modification of absorption profiles[8], or used attosecond streak-field spectroscopy[18] to measure the 2s2p autoionization life time. A 1.2-fs two-electron wave packet formed by the coherent superposition of two autoionizing states was recently predicted theoretically[19].

Our experimental method (Fig. 1a,b; Methods Summary "Experimental Setup"; Methods "Experimental Apparatus Details"; Methods "Experimental Data Acquisition"; Extended Data Fig. 1) exceeds existing attosecond transient-absorption approaches by adding high-spectral-resolution capability with an extreme-ultraviolet (XUV) flat-field grating spectrometer. It allows the parallel measurement of *spectrally narrow* absorption lines imprinted on an attosecond-pulsed *broad-band* XUV spectrum in the presence of a near-visible (VIS) laser field. The VIS laser couples the two-electron excited states (Fig. 1c) either weakly, at low intensities, or strongly, at high intensities. The time-delay between VIS and XUV fields, and the intensity of the VIS field, can be varied as experimental parameters. This creates a novel multi-dimensional transient-coupling scheme, based on the perturbed free polarization decay, well known from femtosecond transient absorption studies[20].

To test the validity of the experimental approach and to support the findings, we performed *ab-initio* theoretical calculations of the attosecond transient-absorption spectra and the two-electron wave-packet motion of the helium atom in a laser field. We employed state-of-the-art methods for the integration of the time-dependent Schrödinger equation on a fully correlated two-electron close-coupling configuration basis (Methods Summary "*Ab-Initio* Simulation"; Methods "*Ab-Initio* TDSE Simulation).

Differential absorption spectra (Methods "Experimental Data Acquisition") for the variation of the VIS–XUV time delay at a low VIS intensity (3×10^{10} W/cm^2) are shown in Fig. 2a,b,c. The excellent agreement between the experimental, the few-level model (Methods "Few-Level Model Simulation"; Extended Data Fig. 2), as well as the *ab-initio* results allows us to fully understand the dynamics in this measurement. The time-resolved absorption change near the two lowest-lying states 2s2p and $sp_{2,3+}$ exhibits a characteristic onset of temporally oscillating structures after time delay 0 with a period of ~1.2 fs. This evidences the creation of coherent two-electron wave-packet dynamics, initiated by the XUV pulse and probed by coupling with the weak VIS pulse. The few-level model confirms the probing mechanism as VIS-induced two-photon dipole coupling of the 2s2p and the $sp_{2,3+}$ states proceeding via the energetically intermediate and spectroscopically dark $2p^2$ state at 62.06 eV (Fig. 1c). While the $2s2p \leftrightarrow 2p^2$ transition alone was previously used to control the transmission of helium[8,12,18], here we measure and exploit the coupling of three autoionizing states for the reconstruction of the two-electron wave packet.

The approximate time-dependent wave function

$$|\Psi(t)\rangle \propto \exp(-\Gamma_{2s2p}/2\, t)|2s2p\rangle + a\, \exp(-\Gamma_{sp23+}/2\, t)\exp(-i\varphi(t))|sp_{2,3+}\rangle$$

is characterized by the relative phase $\varphi(t)$ and amplitude a of the two contributing states 2s2p and $sp_{2,3+}$. The states' slow amplitude decay is given by their respective natural decay width Γ,

accessible from static spectroscopy[15]. The relative amplitude $a = \frac{d_{sp23+}}{d_{2s2p}} \sqrt{\frac{S(\omega_{sp23+})}{S(\omega_{2s2p})}}$ follows directly from their dipole moments d_{2s2p}, d_{sp23+}[21] to the ground state, and the XUV spectrum $S(\omega)$ at the resonance positions ω_{2s2p}, ω_{sp23+}. The relative phase $\varphi(t)$ by contrast is not accessible in traditional spectroscopy. In our time-resolved measurement, different transition pathways involving the doubly-excited states interfere as a function of time, turning $\varphi(t)$ into an experimental observable by analyzing the delay-dependent near-resonance absorption (Methods "Measuring the Wave-Packet Phase in Real/Elapsed Time"; Extended Data Figs. 5&6). The measured phase $\varphi(t)$ is plotted in Fig. 2d/e, and agrees well with the *ab-initio* simulation results. The relative amplitude is given by $a = (0.5 \pm 0.2)$, where the error is mainly due to the fluctuation of the experimental XUV spectrum. The measured values of a and $\varphi(t)$ fully characterize the two-electron wave packet composed of the two autoionizing quantum states $|2s2p\rangle$ and $|sp_{2,3+}\rangle$. By using the known time-independent real-space representations of these states calculated by the complex scaling method[22], we can reconstruct and visualize the wave packet. A section of this time-dependent spatial distribution of the two electrons is shown in Fig. 2f, and compared with the *ab-initio* time-dependent simulation. The agreement is very good and shows that the main features of the two-electron dynamics are dominated by the superposition of the $|2s2p\rangle$ and $|sp_{2,3+}\rangle$ states. Due to the well-defined spectral coherence (i.e. phase locking[23]) present in a high-harmonic spectrum, the observation of a well-defined phase evolution $\varphi(t)$ is possible[24] even in the absence of carrier-envelope-phase stabilization and without knowing the number of attosecond pulses in our few-cycle generated attosecond-pulse train (Methods "Effects of the Attosecond Pules Configuration and the Carrier Envelope Phase"; Extended Data Figs. 4-6). The images (Fig. 2f) clearly show that the two-electron motion in the reconstructed doubly excited wave packet is highly correlated. Direct experimental observation of such concerted dynamics requires the use of coincidence techniques[25-27] and represents a major future goal.

At higher intensities (Methods "Intensity Calibration"; Extended Data Fig. 3) of 3.5×10^{12} W/cm^2 (Fig. 3) a shifting, splitting and broadening of the main absorption lines near zero delay (previously reported in inner-valence excitation of argon[9]) is observed, both in the experiment (Fig. 3a) and in the *ab-initio* simulation (Fig. 3b). The wave-packet motion is still present (fast absorbance modulations even at late delay times) but now significantly affected by the more intense VIS pulse. In addition, near delay time zero, strong delay-dependent modifications of the Fano spectral line shapes of the higher-lying states are observed. The agreement between the experimental data and the *ab-initio* simulation is remarkable.

After understanding and validating our experimental method by measuring the time-dependent relative phase of quantum states in a two-electron wave packet, we proceed to expanding its applicability for general two-electron quantum-state holography and wave-packet control. The electric field strength of the VIS pulse is an important parameter: it controls the coupling strength between the states, and between the states and the continuum. Continuous variation of the VIS pulse intensity thus opens a 3rd spectroscopic dimension (Supplementary Movie 1), in addition to time delay and the spectrum.

Fig. 4a shows the results of VIS laser-intensity tuning in our experiment at a fixed time delay of 5.4 fs. It continuously maps the transition from the unperturbed to the strong-coupling regime of discrete doubly-excited states that is evident near 60 eV. All states are observed to resist the laser electric fields far beyond classical detachment of the outermost electron by overcoming the attractive nuclear Coulomb force (over-the-barrier ionization[28]).

In addition, we observe the continuous change of the Fano line shapes as a function of intensity for all states. As explained in Ref. [13], the line shape of such laser-modified Fano resonances contains information on the phase of the complex dipole response function $d(t)$ after the interaction with the VIS laser pulse. As the $1s^2$ ground state is not significantly affected by the VIS laser at the intensities used here, one can write

$$d_n(t) \propto \langle 1s^2|d|sp_{2,n+}\rangle \exp[-iE_n \cdot t] \exp[i\phi_n],$$

where the dipole phase shift ϕ_n is approximately equal to the relative phase shift φ_n of the quantum state at energy E_n. The excellent agreement between ϕ_n (extracted from the Fano line shape[13]) and φ_n (defining the wave packet) is confirmed by the *ab-initio* simulation in Fig. 4b,e,f. This allows us to experimentally map out the intensity-dependent phase shifts $\varphi_n(I)$ on the quantum states by performing Fano-line-shape analysis (Methods "Line Shape Analysis for Phase Retrieval"; Extended Data Fig. 7). The results are shown in Fig. 4c,d. Since the phase dependence of 2s2p and $sp_{2,3+}$ is opposite in sign, their phase difference can be tuned approximately through a full range of 2π, allowing for the full control of the two-state two-electron wave packet. From the measured laser-induced shift in the phase of each quantum state we can visualize the shape of the wave packet at any time during its field-free evolution. In Fig. 4g,h we show this for the representative real time t = 15.6 fs. Intensity can thus be used as a knob to control the shape of correlated two-electron wave packets at a specific time. In future applications to covalently-bound neutral molecules, the strong-field shaping of two-electron wave packets is a powerful perspective towards laser control of chemical reactions. This further motivates experiments employing coincidence imaging methods (for a review, see e.g. Ref. 25) for direct measurements of the spatial shape of two-(or multi-)electron wave packets as a function of time in the attosecond domain.

The extracted state-dependent phases $\varphi_n(I)$ will allow further insight into the coupling among two electrons and how they, collectively or cooperatively, acquire dynamical phases $\varphi_n(I) = \int \Delta E_n(t) dt$, by time-dependent and state(n)-dependent energy-level shifts $\Delta E_n(t)$ (e.g. Stark or Zeeman shifts) under external perturbation. Having state-resolved access to and control over the full quantum information—amplitude and phase—for two-electron-excited states as a function of time and intensity, more fundamental questions can be addressed in the future: How do two-electron transition states respond to field strengths ranging from the weak- to the strong-field limit? What is the dynamics and fate of doubly-excited states at and before the onset of ionization? What is the validity range of commonly-used[8,18,28] single-active electron pictures for strong-field ionization of few-electron systems? The answers carry important consequences for scientific dreams and visions, e.g. to create synthetic atomic quantum systems and exotic molecules beyond the reaches of traditional chemistry by ultrafast temporally tailored light fields[29].

Methods Summary

Experimental Setup

A few-cycle amplified laser system (Femtolasers Compact Pro) with hollow-fibre and chirped-mirror compression stages delivers 5-7 fs pulses at a 4 kHz repetition rate. These pulses are coupled into our home-built attosecond interferometry vacuum beamline (Fig. 1; Extended Data Fig. 1a; Methods "Experimental Apparatus Details") consisting of a XUV source chamber, refocusing and time-delay chamber and a target chamber followed by a high-resolution ($\Delta\lambda$ = 0.01 nm, corresponding to ΔE = 20 meV near ~60 eV) XUV spectrometer. Trains of few attosecond XUV pulses with ~600 as duration are generated by the intrinsically phase locked[23] broadband harmonics in the relevant region of 60-65 eV by high-order harmonic generation (HHG) in a gas cell filled with neon (~100 mbar). The generated XUV pulses then co-propagate with their intense driver pulse and impinge at 15-degree grazing-incidence angle on a two-component split mirror. The XUV pulses reflect off a smaller inner mirror (centred

on the optical axis) while the more divergent VIS pulses are reflected by a larger outer mirror surrounding the inner mirror. The inner mirror can be translated parallel to its surface normal to create high-precision (10 as) time delays between the XUV attosecond and VIS femtosecond pulses. Inserting an aluminium filter and a polymer membrane with a centre hole, we create an annular femtosecond VIS laser beam that is fully separable in time (delay) and space from the inner attosecond XUV beam. These pulses are then focused into a second gas cell of 3 mm length—providing the helium used in this study at a pressure of 100 mbar—using a toroidal mirror (focal length 0.35 m) under 15° grazing angle. The VIS pulse intensity is tuned by a motor-controlled iris aperture before focusing into the helium target. The focus in the gas cell also represents the entrance slit of our flat-field (variable-line-space grating) spectrometer, recording the absorption spectrum in the range between 20 and 120 eV.

Ab-Initio Simulation

The *ab-initio* transient absorption spectrum is reproduced using the velocity-gauge perturbative expression $\sigma_{TAS}(\omega) = 4\pi\omega^{-1}\mathrm{Im}[\,\tilde{p}(\omega)/\tilde{A}(\omega)\,]$, where ω is the field angular frequency, $\tilde{p}$ and $\tilde{A}$ are the Fourier transform of the expectation value of the total canonical electronic momentum $p(t) = \langle\psi(t)|p_z|\psi(t)\rangle$, and of the XUV vector potential amplitude, respectively, and $\psi(t)$ is the wave function for the helium atom in the presence of the external field. $p(t)$ is obtained by direct integration of the time-dependent Schrödinger equation (TDSE), $i\partial_t\psi(t) = \left[H_0 + V_{abs} + \alpha\vec{A}(t)\cdot\vec{p}\right]\psi(t)$ where H_0 is the field-free electrostatic Hamiltonian of helium, $\alpha\vec{A}(t)\cdot\vec{p}$ is the velocity-gauge minimal-coupling dipole term, and V_{abs} is a complex potential that prevents reflection from the quantization-box boundaries. The wave function is expanded on the eigenstates of H_0 projected on a two-particle B-spline close-coupling basis with pseudostates[30]. The TDSE is integrated numerically with a second-order mid-point exponential time-step propagator[19]. In the simulation, we include states with total angular momentum up to $L_{max} = 10$ and, for the localized cannel, orbital angular momentum up to $l_{max} = 5$. The external field comprises two linearly polarized pulses: a) a gaussian XUV pulse with duration (intensity FWHM) 380 as, central energy 61.3 eV, and intensity $I = 10^{11}$ W/cm^2; b) a cosine-square VIS pulse with duration of 7 fs, central energy 1.7 eV, intensity ranging from 0 to 10 TW/cm^2, and time delay with respect to the XUV pulse variable from -15 to 35 fs. To compare with the wave packets reconstructed from the experiment, the spatial part of the wave function is tabulated as a function of z_1 and z_2 with both electrons aligned to the field polarization axis, for selected pump–probe time delays and observation times.

Online Content Methods, along with any additional Extended Data display items are available in the online version of the paper; references unique to these sections appear only in the online paper.

References

1. Pisharody,S.N. & Jones,R.R. Probing two-electron dynamics of an atom. *Science* **303**, 813-815 (2004).

2. Vanroose,W., Martin,F., Rescigno,T.N. & McCurdy,C.W. Complete photo-induced breakup of the H-2 molecule as a probe of molecular electron correlation. *Science* **310**, 1787-1789 (2005).

3. Remacle,F. & Levine,R.D. An electronic time scale in chemistry. *Proc. Nat. Acad. Sci. USA* **103**, 6793-6798 (2006).

4. Lin,C.D. Hyperspherical coordinate approach to atomic and other Coulombic three-body systems. *Physics Reports* **257**, 2-83 (1995).

5. Goulielmakis,E. *et al.* Real-time observation of valence electron motion. *Nature* **466**, 739-744 (2010).

6. Mauritsson,J. *et al.* Attosecond Electron Spectroscopy Using a Novel Interferometric Pump-Probe Technique. *Phys. Rev. Lett.* **105**, 053001 (2010).

7. Holler,M., Schapper,F., Gallmann,L. & Keller,U. Attosecond Electron Wave-Packet Interference Observed by Transient Absorption. *Phys. Rev. Lett.* **106**, 123601 (2011).

8. Loh,Z.H., Greene,C.H. & Leone,S.R. Femtosecond induced transparency and absorption in the extreme ultraviolet by coherent coupling of the He 2s2p (P-1(o)) and 2p(2) (S-1(e)) double excitation states with 800 nm light. *Chem. Phys.* **350**, 7-13 (2008).

9. Wang,H. *et al.* Attosecond Time-Resolved Autoionization of Argon. *Phys. Rev. Lett.* **105**, 143002 (2010).

10. Lambropoulos,P. & Zoller,P. Autoionizing States in Strong Laser Fields. *Phys. Rev. A* **24**, 379-397 (1981).

11. Themelis,S.I., Lambropoulos,P. & Meyer,M. Ionization dynamics in double resonance involving autoionizing states in helium: the effect of pulse shapes. *J. Phys. B* **37**, 4281-4293 (2004).

12. Chu,W.C., Zhao,S.F. & Lin,C.D. Laser-assisted-autoionization dynamics of helium resonances with single attosecond pulses. *Phys. Rev. A* **84**, 033426 (2011).

13. Ott,C. *et al.* Lorentz Meets Fano in Spectral Line Shapes: A Universal Phase and Its Laser Control. *Science* **340**, 716-720 (2013).

14. Meyer,H.D., Manthe,U. & Cederbaum,L.S. The Multi-Configurational Time-Dependent Hartree Approach. *Chem. Phys. Lett.* **165**, 73-78 (1990).

15. Schulz,K. *et al.* Observation of new Rydberg series and resonances in doubly excited helium at ultrahigh resolution. *Phys. Rev. Lett.* **77**, 3086-3089 (1996).

16. Beutler,H. Über absorptionsserien von argon, krypton und xenon zu termen zwischen den beiden ionisierungsgrenzen 2 *P*3 2/0 und 2*P*1 2/0. *Z. Phys. A* **93**, 177-196 (1935).

17. Fano,U. Effects of Configuration Interaction on Intensities and Phase Shifts. *Phys. Rev.* **124**, 1866-1878 (1961).

18. Gilbertson,S. *et al.* Monitoring and Controlling the Electron Dynamics in Helium with Isolated Attosecond Pulses. *Phys. Rev. Lett.* **105**, 263003 (2010).

19. Argenti,L. & Lindroth,E. Ionization Branching Ratio Control with a Resonance Attosecond Clock. *Phys. Rev. Lett.* **105**, 053002 (2010).

20. Pollard,W.T. & Mathies,R.A. Analysis of Femtosecond Dynamic Absorption-Spectra of Nonstationary States. *Annu. Rev. Phys. Chem.* **43**, 497-523 (1992).

21. Rost,J.M., Schulz,K., Domke,M. & Kaindl,G. Resonance parameters of photo doubly excited helium. *J. Phys. B* **30**, 4663-4694 (1997).

22. Reinhardt,W.P. Complex Coordinates in the Theory of Atomic and Molecular-Structure and Dynamics. *Annu. Rev. Phys. Chem.* **33**, 223-255 (1982).

23. Paul,P.M. *et al.* Observation of a train of attosecond pulses from high harmonic generation. *Science* **292**, 1689-1692 (2001).

24. Kim,K.T. *et al.* Amplitude and Phase Reconstruction of Electron Wave Packets for Probing Ultrafast Photoionization Dynamics. *Phys. Rev. Lett.* **108**, 093001 (2012).

25. Ullrich,J. *et al.* Recoil-ion and electron momentum spectroscopy: reaction-microscopes. *Rep. Prog. Phys.* **66**, 1463 (2003).

26. Morishita,T., Watanabe,S. & Lin,C.D. Attosecond Light Pulses for Probing Two-Electron Dynamics of Helium in the Time Domain. *Phys. Rev. Lett.* **98**, 083003 (2007).

27. Palaudoux,J. *et al.* Multielectron spectroscopy: Auger decays of the krypton 3d hole. *Phys. Rev. A* **82**, 043419 (2010).

28. Augst,S., Meyerhofer,D.D., Strickland,D. & Chin,S.L. Laser Ionization of Noble-Gases by Coulomb-Barrier Suppression. *J. Opt. Soc. Am. B* **8**, 858-867 (1991).

29. Assion,A. *et al.* Control of chemical reactions by feedback-optimized phase-shaped femtosecond laser pulses. *Science* **282**, 919-922 (1998).

30. Argenti,L. & Moccia,R. K-matrix method with B-splines: sigma (nl), beta(n) and resonances in He photoionization below N=4 threshold. *J. Phys. B* **39**, 2773-2790 (2006).

Supplementary Information is linked to the online version of the paper at www.nature.com/nature.

Acknowledgements We thank E. Lindroth for calculating the dipole moment $\langle 2p^2|\mathbf{r}|sp_{2,3+}\rangle$, and also A. Voitkiv, Z.-H. Loh, and R. Moshammer for helpful discussions. We acknowledge financial support by the Max-Planck Research Group Program of the Max-Planck Gesellschaft (MPG) and the European COST Action CM1204 XLIC. L. A. and F. M. acknowledge computer time from the CCC-UAM and Mare Nostrum supercomputer centers and financial support by the European Research Council under the ERC Advanced Grant no. 290853 XCHEM, the Ministerio de Economía y Competitividad projects FIS2010-15127, FIS2013-42002-R and ERA-Chemistry PIM2010EEC-00751, and the European grant MC-ITN CORINF.

Author Contributions C.O. and T.P. designed the experiment. C.O., A.K., P.R., R.H., and T.P. built the experimental apparatus. C.O., A.K., Y.Z., P.R., and T.P. conducted the experiments. C.O., A.K., S.H., R.H., and T.P. performed the experimental data analysis and interpretation, C.O., A.K., S.H., T.D., R.H, and T.P. carried out the few-level model simulation. L.A. and F.M. carried out the *ab-initio* simulation and significantly contributed to the interpretation of the

results. J.M. calculated the field-free wave functions. C.O., A.K., L.A., F.M., and T.P. created major parts of the manuscript. All authors contributed to the discussion of the results and commented on the manuscript.

Author Information Reprints and permissions information is available at www.nature.com/reprints. The authors declare no competing financial interests. Readers are welcome to comment on the online version of this article at www.nature.com/nature. Correspondence and requests for materials related to the experiment and the few level model should be addressed to C.O. (christian.ott@mpi-hd.mpg.de), or T.P. (thomas.pfeifer@mpi-hd.mpg.de), and those related to the ab initio calculations to L.A. (luca.argenti@uam.es) or F. M. (fernando.martin@uam.es)

Figure Legends

Figure 1 | Illustration of the experimental setup, data, and microscopic mechanisms in helium. a, Few-cycle (7 fs) VIS laser pulses (730 nm) are focused into a neon gas cell for partial attosecond-pulse conversion, providing a continuous coherent excitation spectrum throughout the XUV range. The time delay between the co-propagating VIS and XUV pulses is controlled by a split(inlay)-mirror stage. Both pulses transit the helium gas target and enter the high-resolution spectrometer. **b,** Absorption spectra without (upper) and in the presence of the VIS laser pulse (lower), throughout the region of the $|sp_{2,n}\rangle$ doubly-excited states. **c,** Helium level diagram: The $|sp_{2,n}\rangle$ states couple to the $|1s,\varepsilon\rangle$ continuum by configuration interaction V_{CI} (green wavy lines). The VIS laser field (red wavy lines) creates an additional time- and intensity-dependent coupling. **d**, The XUV pulses can either directly ionize He to He^+, or excite both electrons into an intermediate transition state, which decays by configuration interaction V_{CI} into He^+, quantum interfering with the direct ionization process (left, natural process). If a laser field is present (right), it shifts the phase of one arm of this natural interferometer—the two-electron transition state—modifying the Fano line shapes detected in the transmitted absorption spectrum. This provides state-resolved experimental access to a quantum phase shift.

Figure 2 | Observation of attosecond two-electron dynamics in helium. a, b, c, Absorption change (ΔOD) of XUV light in helium versus time delay between the VIS (3×10^{10} W/cm^2 intensity) coupling field and the XUV pulse. (**a**): Experiment, (**b**): few-level model simulation, and (**c**): *ab-initio* calculation show the onset of temporal oscillations near $\tau = 0$ and persisting to large positive delays. **d**, Oscillation of ΔOD vs. time delay τ near resonance at 63.67 eV. **e,** Modulation phase $\varphi_{OD}(\tau)$ of $\Delta OD(\tau)$ and relative phase $\varphi(t)$ of the XUV-pulse-induced two-electron wave packet involving the 2s2p, and $sp_{2,3+}$ states, reconstructed by applying to $\varphi_{OD}(\tau)$ a small systematic phase shift (Methods "Measuring the Wave-Packet Phase in Real/Elapsed time"). The inset shows the experimentally retrieved phase $\varphi(t)$ relative to the theoretical expectation. The error bars in (d/e) reflect the statistical noise of the measured absorption spectra. **f,** Visualization of the two-electron wave packet motion. Snapshots of the correlated quantum probability distribution along a line through the helium atom is shown at several instants of elapsed time *t*. Left column: experimentally reconstructed wave packet including only the two measured states 2s2p and sp_{23+}. Right column: *ab-initio* 3D TDSE simulation, including all excited states.

Figure 3 | Time-delay dependent absorption at higher VIS intensity (3.5×10^{12} W/cm^2). a, Time-resolved experimental absorption spectrum in OD (optical density) at a higher VIS intensity of 3.5×10^{12} W/cm^2: At negative delays the static Fano profile[17] is measured for several autoionizing states up to $sp_{2,7+}$. Near temporal overlap and at positive delays, the absorption spectrum is strongly modified. At slightly positive delays a clear signature of Autler-Townes splitting of the 2s2p resonance with the energetically repelling $2p^2$ dressed state is measured at ~60 eV, confirming the strong-coupling regime of autoionizing states and multiple Rabi cycling between these two states. **b,** The full *ab-initio* simulation shows excellent agreement with the experiment, thus providing further proof of the existence of a well-defined two-electron wave packet even at higher VIS intensities.

Figure 4 | Intensity-dependent laser coupling and phase control of a two-electron wave packet. a, XUV absorption spectra at a time delay of +5.4 fs for increasing VIS coupling intensity. Near 60 eV we continuously follow the transition from the unperturbed to the two-electron strong-coupling regime of the 2s2p with $2p^2$ and $sp_{2,3+}$. **b,** Absorption spectra calculated with the *ab-initio* simulation as a function of the VIS intensity at a time delay of +4.8 fs. **c,d:** Reconstruction of the intensity-dependent temporal phase change of the 2s2p and $sp_{2,3+}$ states after their interaction with the VIS pulse, retrieved via Fano line-shape analysis[13] (Methods "Line-Shape Analysis for Phase Retrieval"; Extended Data Fig. 7). The state-dependent change of the phase as a function of the intensity demonstrates laser-controlled manipulation of the two-electron dynamics (**g**), shown in 2D representation at a representative time t = 15.6 fs after the XUV pulse. **e,f:** Reconstruction of the intensity-dependent phase change in the *ab-initio* simulation for the same states as in (c,d), again using Fano line-shape analysis (black solid line). The red dots mark the phase shift of the coefficients, read out after the laser pulse. The excellent agreement with the phase extracted from line-shape analysis (experimentally accessible observable) validates this phase-reconstruction method. **h:** two-electron probability distribution as obtained from the *ab-initio* simulation, for the same time and intensity parameters as in (g).

Online Methods

Experimental Apparatus Details. The laser system (commercial Ti:Sapphire multipass amplifier "Femtolasers Compact Pro"; hollow-core fiber spectral broadening; temporal pulse compression with chirped mirrors) typically delivers sub-7-fs, ~730 nm, 0.3 mJ laser pulses at 4 kHz repetition rate. The carrier-envelope phase (CEP) was not stabilized but averaged over to avoid additional fluctuations from CEP noise in the high-harmonic spectrum, especially since our measurement scheme is insensitive to the CEP (see Methods, section "Effects of the Attosecond Pulse Configuration and the Carrier Envelope Phase"). The vacuum setup is shown in Extended Data Fig. 1a. The laser pulses were focused (50 µm focal spot size; peak intensities 10^{14} to 10^{15} W/cm^2) into a stainless-steel cell filled with neon gas, entering and exiting through 100 µm diameter machine-drilled holes in the cladding. A small fraction of the visible (VIS) light was up-converted into the extreme ultraviolet (XUV) energy range, using high-harmonic generation (HHG) for attosecond pulse production[32]. The macroscopic parameters were optimized for continuous spectra (100 mbar neon backing pressure; cell position near the laser focus). In Extended Data Fig. 1b, a typical XUV spectrum is shown, alongside an XUV spectrum after transmission through a 100 mbar helium gas target. The co-propagating XUV and VIS

pulses were separated by a 2 μm thin silicon nitride membrane with a ~2 mm diameter centre hole, in combination with a concentrically mounted 200 nm thin aluminium filter behind the hole. This separation scheme is making use of the intrinsically lower divergence of the XUV beam. The time delay between the XUV and VIS pulses was obtained by a grazing-incidence (15°) split-mirror setup consisting of an inner gold-coated mirror (2 mm size) for the XUV, and a surrounding silver mirror for the VIS. The inner mirror can be translated with respect to the outer mirror using a high-precision piezo stage (~1 nm resolution; ~260 μm range). Both beams were refocused (1:1 geometry; 350 mm focal length) with a gold-coated toroidal mirror under the same 15° grazing angle of incidence into another stainless-steel cell filled with helium gas. The monolithic setup guarantees a high interferometric stability (measured temporal precision ~10 as), combined with broadband and high-throughput advantages of all-grazing-incidence optics. Spectral selection was achieved by thin metal filters (200 nm thin aluminium), transmitting in the 20 to 70 eV energy range[33]. The intensity of the VIS beam on the helium target was finely tuned using a picomotor-controlled iris diaphragm centred around both beams. The XUV radiation transmitted through the helium target was spectrally imaged with a flat-field spectrometer consisting of a variable line spacing (VLS) grating and a thermoelectrically-cooled, back-illuminated XUV CCD camera. The VIS stray light was removed with a pair of 200 nm thin aluminium metal filters. The spectrometer calibration was obtained by identifying the observed $sp_{2,n+}$ two-electron resonance lines in helium and using tabulated experimental values of high-precision synchrotron measurements[34,15]. The spectral resolution (σ = 20 meV Gaussian standard deviation) near 60 eV resulted from a fit of the 2s2p resonance line. The target gas density (~100 mbar) was chosen such that the strongest 2s2p absorption line was still well below OD 2 to avoid dispersion and propagation effects[35]. The zero position of time delay was obtained by generating high harmonics in argon in the target gas cell, and accounting for the known thickness of the silicon nitride membrane and the aluminium filter.

Experimental Data Acquisition. Sets of XUV spectra were recorded as a function of time delay (from −18 to +34 fs in ~170 as steps, negative values correspond to VIS pulse arriving first) and VIS intensity (35 different iris diaphragm opening settings up to the 10^{12} W/cm^2 peak-intensity regime), where the intensity calibration was obtained *in-situ* as described below (see Methods, section "Intensity Calibration"). Each single spectrum was obtained by integration over ~3200 laser shots. For each VIS intensity, additional XUV spectra were recorded without the target helium gas to obtain reference spectra (Extended Data Fig. 1b). The absorbance A, also known as optical density (OD), is obtained by the general formula $A = -\log_{10}(I_{SIG}/I_{REF})$, with the background-corrected signal (I_{SIG}) and reference (I_{REF}) spectral intensity. At an exemplary VIS intensity of 3.3×10^{12} W/cm^2, the two-dimensional absorbance, plotted vs. time delay and photon energy, is displayed in Extended Data Fig. 1c. All relevant structures as discussed in the main text can already be seen. The noisy structures (horizontal lines) are a result of the non-simultaneous measurement of signal and reference XUV spectra, and were filtered out for our quantitative analysis using the following method: For each recorded signal XUV spectrum (containing absorption lines), a low-pass Fourier filter was employed to filter out the "slowly" modulating (~3.4 eV period) high-harmonic XUV spectrum. This *in-situ* filtered spectrum $I_f(\omega)$ was scaled to obtain a reconstructed reference spectrum $I_{REF,rc}(\omega)$ by using Beer's law, $I_{REF,rc}(\omega) = I_f(\omega)\cdot\exp[\sigma_{PCS}(\omega)\cdot l\cdot\rho]$, with the known non-resonant photo-absorption cross-section

σ_{PCS} of helium[36]. The path length density product $l \cdot \rho$ is the free scaling parameter and was determined to $l \cdot \rho = (0.56 \pm 0.05) \times 10^{18}$ cm^{-2} via comparison to the measured spectral intensity I_{REF}. As a result of this reference-reconstruction method, the noise of the two-dimensional absorbance plots is significantly reduced, as can be seen by comparing Extended Data Fig. 1c to Fig. 3a in the main text. The differential absorption spectra shown in Fig. 2 in the main text were generated by subtracting the field-free (no VIS laser) static spectra, plotting the absorption change of the optical density (ΔOD).

Few-Level Model Simulation. The model system consists of three autoionizing states 2s2p (^{1}P^o), 2p^2 (^{1}S^e), and sp$_{2,3+}$ (^{1}P^o) at excitation energies 60.15 eV, 62.06 eV and 63.66 eV, resp., above the 1s^2 (^{1}S^e) helium ground state[34,37]. Other states belonging to the $N = 2$ doubly-excited Rydberg series are off-resonant to the coupling VIS laser (~1.7 eV photon energy) and/or significantly lower in coupling strength, and are thus neglected. This sub-system of states is sufficient to reproduce the experimentally observed 1-fs quantum beat. The model is based on previous work by Lambropoulos *et al.*[10,11], solving the time-dependent Schrödinger equation in the configuration basis of the VIS-coupled states. The parity-allowed (^{1}S$^e \leftrightarrow ^1$P^o) transitions are expressed by the dipole matrix elements d_{nm} as depicted in Extended Data Fig. 2a, which also includes the configuration interaction matrix elements $V_{\varepsilon,n}$ that connect the autoionizing states to their respective single-electron continua |1sεs> or |1sεp>. In accordance with earlier approaches for a similar system[11], the non-resonant VIS-induced coupling of the ^{1}P^o states with the |1sεs> continuum is neglected. Also the VIS coupling between the two continua can be safely neglected in our intensity regime[10]. Extended Data Fig. 2b depicts the Schrödinger equation of the so described few-level system, with the states' complex expansion coefficients $c_n(t)$, and using atomic units (a.u.). The weak excitation with the broadband XUV field $F_{\mathrm{XUV}}(t)$ is described in first-order perturbation theory, i.e., $\partial_t c_g(t) = 0$, with $E_g = 0$. Under the rotating wave approximation, $F_{\mathrm{XUV}}(t)$ is taken as a complex quantity, neglecting the anti-resonant part of interaction. The coupling between the excited bound states is mediated with the full time-dependent real representation of the VIS field $F_{\mathrm{VIS}}(t)$. The continua are treated in strong-field approximation as Volkov states with the vector potential $A_{\mathrm{VIS}}(t) = -\int_{-\infty}^{t} \mathrm{d}t' \, F_{\mathrm{VIS}}(t')$ and are parameterized with their kinetic momentum p. A one-dimensional treatment is justified due to the linear polarization of the electric fields. The continuum states are described as quasi-discrete non-interacting states separated by Δp. To suppress continuum revivals which are an artefact of this discretization, a constant decay rate γ is employed which spectrally broadens the quasi-discrete states to a mutual overlap. The configuration-interaction matrix elements $V_{\varepsilon,n} = \langle 1s,\varepsilon p/s|\mathbf{H}|n\rangle \equiv V_n$, which describe autoionization, are taken to be constant (i.e. energy independent) in the vicinity of each configuration state, in accordance with Fano's original theory[17].

Direct numerical integration of the time-dependent complex expansion coefficients $c_n(t)$ was performed with a split-step-like approach, where for each time interval Δt, different sub-systems were evaluated separately. The corresponding five steps were: i) The perturbative excitation of states |a>, |c>, and the set of |1s,εp> continuum states in the XUV laser field. ii) The coupling of the three bound states |a>, |b> and |c> in the VIS laser field. iii) The coupling of the three bound states |n> with their corresponding continuum states |1s,εp/s> due to configuration interaction. iv) The field-free evolution of the three bound states with eigenenergies E_n. v) The VIS laser-

dressed evolution of the quasi-discrete continuum states. For each of these five steps, the corresponding sub-system was diagonalized, thus temporal evolution corresponds to the multiplication of a complex phase factor "$\exp(-i\lambda_j \cdot \Delta t)$" with λ_j being the eigenvalues of the diagonalized sub-system after a unitary transformation. For each time point, the time-dependent dipole moment $D(t)=d_{ga}\cdot c_a(t)+d_{gc}\cdot c_c(t)+d_g\cdot\sum_\varepsilon c_{\varepsilon p}(t)$ between the ground state |g> and the dipole-allowed |a/c> states as well as the |1s,εp> continuum states was evaluated, where the ground–continuum dipole matrix element $d_g \equiv d_{g\varepsilon}$ was assumed independent of energy. The absorption spectra were calculated[20] via the Fourier transform of $D(t)$, which is proportional to the polarization $P(\omega)$ of the system. Dividing this quantity by the XUV laser spectrum $F(\omega)$ (to obtain a quantity which, in the absence of the VIS field, is proportional to the susceptibility $\chi(\omega)$ of helium, where $P(\omega) = \varepsilon_0 \chi(\omega)F(\omega)$; in the presence of the VIS field this corresponds to a generalized linear susceptibility as discussed in Ref. 20) and taking the imaginary part of this ratio lead to the XUV absorption profile. This quantity is proportional to the experimentally reconstructed absorbance as introduced in Methods, section "Experimental Data Acquisition", in our limit of low absorption and thus negligible propagation/dispersion effects.

The used numerical parameters were: discretization time step Δt = 1 a.u. (0.0242 fs); total time of simulation T = 32000 a.u. (774 fs); discretized single-electron continuum from p_{min} = ±1.35 a.u. (i.e. E_{min} = 24.8 eV) to p_{max} = ±2.80 a.u. (i.e. E_{max} = 106.7 eV) in 100 steps with Δp = ±0.0145 a.u. (i.e. in total 400 quasi-discrete continuum states), with decay rate γ = 0.1 a.u.; energies, widths and asymmetry parameters of $^1P^o$ states[15,34] E_a = 60.147 eV, Γ_a = 37 meV, q_a = –2.75, and E_c = 63.658 eV, Γ_c = 10 meV, q_c = –2.53; energy and width of $^1S^e$ state[37,38] E_b = 62.06 eV and Γ_b = 6 meV; dipole matrix element d_{ab} = 2.17 a.u. was taken from Ref. 8, while d_{bc} = –0.81 a.u. was calculated[39]. The remaining V_n, d_{gn} and d_g were determined for the simulated absorption spectra to match known experimental and theoretical line shapes with above printed values. The laser pulses were defined as $F^{(0)}\exp[-(t/t_G)^2]\cos(\omega_c t+\varphi_{CEP})$, with the peak electric field strength $F^{(0)}$, the Gaussian pulse duration $t_G = t_p/\sqrt{[2\ln 2]}$ where t_p denotes the full width at half maximum (FWHM) intensity, the center frequency ω_c and the carrier-envelope phase (CEP) φ_{CEP}. The time discretization and total time simulated allowed to correctly describe all dynamics in a reasonable amount of computation time (narrowest line width of Γ_b = 6 meV corresponds to ~110 fs life time). The decay rate γ effectively maintains the autoionized electrons for ~16 Bohr radii a_0, which is a reasonable upper estimate for the spatial extend of the localized two-electron states.

The simulation was validated by employing a quasi-monochromatic ($t_G >> T$) VIS laser field (λ ~ 730 nm) of increasing field strength $F^{(0)}_{VIS}$, where the obtained cycle-averaged absorbance is depicted in Extended Data Fig. 2c. As expected, line splitting and AC Stark shifts according to the Rabi frequency $d_{nm}\cdot F^{(0)}_{VIS}$ occur due to Rabi cycling among the three states. The temporal evolution of their coefficients is shown in Extended Data Fig. 2d-f at various time delays, where a 7 fs VIS laser pulse was applied instead. Significant rearrangement of population between the states occurs which is maintained at times after the VIS pulse interaction. This intuitively illustrates how the VIS laser pulse affects the relative population of the two-electron states, which is experimentally accessible in the measured absorption line shapes since these are derived from the oscillating dipole moment $D(t)$. The few-level model simulation was used i) for the reconstruction of the experimentally observed two-electron wave packet which allowed for an

independent comparison with the full *ab-initio* 3D TDSE calculation, and ii) to check for possible effects of various different pulse configurations on the investigated dynamics.

***Ab Initio* TDSE Simulation.** The *ab initio* transient absorption spectrum was reproduced using the velocity-gauge perturbative expression

$$\sigma_{TAS}(\omega) = \frac{4\pi}{\omega}\mathrm{Im}\frac{\tilde{p}(\omega)}{\tilde{A}(\omega)} \qquad (1)$$

where ω is the field angular frequency, $\tilde{p}$ is the Fourier transform of the total electronic canonical momentum expectation value,

$$\tilde{p}(\omega) = \frac{1}{\sqrt{2\pi}}\int_{-\infty}^{\infty} \mathrm{d}t e^{-i\omega t} p(t), \qquad p(t) = \langle \psi(t) | p_z | \psi(t) \rangle, \qquad (2)$$

$\tilde{A}$ is the Fourier transform of the XUV vector potential amplitude, and $\psi(t)$ is the wave function for the helium atom in the presence of the external field. The use of Eq. (1) is justified in the limit of optically thin samples. Already for VIS pulse intensities of the order of few TW/cm^2, the optical response $p(t)$ depends non-perturbatively on the VIS external field. For this reason, $p(t)$ was obtained integrating the time-dependent Schrödinger equation (TDSE),

$$i\partial_t \psi(t) = \left[H_0 + V_{abs} + \alpha \vec{A}(t)\cdot\vec{p}\right]\psi(t), \qquad (3)$$

where H_0 is the field-free electrostatic Hamiltonian of helium, $\alpha\vec{A}(t)\cdot\vec{p}$ is the minimal-coupling term that accounts for the interaction of the atom with the external field, and V_{abs} is a symmetric complex local potential that prevents reflection from the boundary of the quantization box where the wave function is defined. To solve the TDSE accurately, the wave function was expanded on the eigenstates of H_0, projected on a two-particle B-spline close-coupling basis with pseudostates[30,31]. In such basis, the angular part is represented by bipolar spherical harmonics and the radial part by B-splines with an asymptotic knot spacing of 0.5 au. Each total angular momentum comprises all the partial-wave channels with configurations of the form $Nl\varepsilon_{l'}$ with $N \leq 2$, and a full-CI localized channel *nln'l'* that reproduces short-range correlations between the two electrons. In the presence of the field, the TDSE was integrated numerically with a second-order mid-point exponential time-step propagator[19],

$$\psi(t+dt) = e^{-iV_{abs}} e^{-iH_0 dt/2} e^{-idt\alpha\vec{A}(t+dt/2)\cdot\vec{p}} e^{-iH_0 dt/2} \psi(t). \qquad (4)$$

The action of the second exponential, which depends on the external fields and couples blocks with different symmetry, is evaluated with an iterative Krylov-space method. In the simulation, we included states with total angular momentum up to $L_{\max} = 10$ and, for the localized cannel, orbital angular momentum up to $l_{\max} = 5$. We ascertained the convergence of the theoretical results with respect to the most relevant expansion parameters in the state representation by conducting additional representative simulations with either $L_{\max} = 15$ or $l_{\max} = 10$, as well as by including the $N = 3$ partial-wave channels in the close-coupling expansion. After the external field is over, the Hamiltonian does not depend on time anymore and the propagation becomes trivial,

$$\psi(t) = \sum_i \left|\varphi_{R,i}\right\rangle e^{-iE_i(t-t')} \left\langle\varphi_{L,i}\right|\left.\psi(t')\right\rangle, \qquad (5)$$

where the states $\varphi_{L/R}$ are the left and right eigenstates of the quenched Hamiltonian $H_Q = H_0 + V_{abs}$, whose complex eigenvalues E_i have non-positive imaginary components,

$$H_Q = \sum_i \left|\varphi_{R,i}\right\rangle E_i \left\langle\varphi_{L,i}\right|, \qquad \left\langle\varphi_{L,i}\middle|\varphi_{R,j}\right\rangle = \delta_{ij}, \qquad \mathrm{Im}\, E_i \le 0 \;\forall\, i\,. \qquad (6)$$

The expectation value $p(t)$ can conveniently be split in two smooth components,

$$p(t) = p^-(t) + p^+(t), \qquad (7)$$

defined in such a way that $p^-(t)$ becomes negligible shortly after the external field is over, while $p^+(t)$ vanishes before and during the presence of the external field. As a result of the separation, the FT of $p(t)$ also splits into the sum of two terms,

$$\tilde{p}(\omega) = \tilde{p}^-(\omega) + \tilde{p}^+(\omega)\,. \qquad (8)$$

The first FT was evaluated numerically from tabulated values of $p(t)$ on a dense time grid. The second FT, instead, was evaluated analytically from (i) the spectral resolution of the quenched Hamiltonian, (ii) the dipole transition matrix elements from the ground state, and (iii) the expansion coefficients of the wave function at a given time after the external fields are over on the numerical basis used to conduct the time propagation. This way of proceeding provides the same result of an infinite time propagation. To compare with the wave packets reconstructed from the experiment, the spatial part of the theoretical wave function $\psi(z_1,z_2;t)$ was tabulated as a function of the cartesian coordinates z_1 and z_2 when both the electrons are aligned to the field polarization axis, for selected pump−probe time-delays and observation times.

Intensity Calibration. The simulated few-level dynamics, which is in good qualitative and quantitative agreement with the experimental data and thus well understood, was used for assessing the intensity of the VIS pulse in the interaction region. Both for the numerical and experimental results, a small temporal region (averaged over two modulation periods) around 0 fs and around ~5 fs time delay (where the Autler–Townes splitting of the 2s2p–$2p^2$-doublet is strongest, for the numerical results this was ~3 fs) was averaged and plotted as a function of the VIS intensity (in the simulation) and iris diaphragm openings (in the experiment), respectively (see Extended Data Fig. 3a,b). By quantifying the induced AC Stark shifts of the light-induced 2s2p–$2p^2$ Autler–Townes doublet in the experiment, and comparing these shifts to the simulated data (based on the known and experimentally confirmed[8] dipole matrix element between the two states) an *in-situ* intensity calibration was achieved, shown in Extended Data Fig. 3c. The calibration includes an average over various VIS pulse durations (ranging from 5 to 30 fs) to account for the effect of a >7 fs pedestal in the VIS pulse, which is typical of the hollow-fiber/chirped-mirror pulse compression method employed.

Effects of the Attosecond Pulse Configuration and the Carrier Envelope Phase. The experimental data was obtained by averaging over the CEP. In addition, the coherent XUV excitation spectrum consisted of a train of few attosecond pulses, which is indicated by energy modulations on top of the broad XUV spectra as shown in Extended Data Fig. 1b. Both these

effects are negligible for the observation of the discussed effects as will be shown in the following. Three different XUV pulse configurations have been simulated and are plotted in Extended Data Fig. 4a, showing no significant changes in the absorbance spectra. This is a direct consequence of the well-known[23] phase locking of the attosecond pulses to the half cycles of the generating intense VIS pulses. In the energy domain, this corresponds to a well-defined coherent excitation spectrum over a broadband spectral range. The insensitivity to the XUV pulse configuration was also confirmed experimentally by performing measurements with and without CEP stabilization. Comparing the corresponding plots in Extended Data Fig. 3b, the additional CEP stabilization in the experiment does not modify the results obtained in the absence of CEP stabilization. Thus, to avoid any sources of error from an imperfect absolute CEP determination (as it currently does not exist for transient-absorption measurements), CEP temporal drift correction, spatial effects such as potential inhomogeneity across the beam profile, or Gouy phase slips at the exact experimental interaction region (extended He target cell), we took the bulk of our data in the well-reproducible situation of non-stable (and thus fully statistical) CEP. We also confirmed the insensitivity of the measurement to the exact pulse-train configuration in the weak-field VIS interaction case for which we extracted the wave-packet phase information shown in Fig. 2 of the main text. The results for single, double, and multi-attosecond-pulse excitation situations are shown in Extended Data Fig. 5. For the definition of the attosecond pulse and its time of arrival with respect to the (generating) VIS laser pulse we used the coherence (phase locking) between two harmonics, which has been confirmed numerous times to be present in high-harmonic generation since its first direct measurement via interferometric two-photon photoelectron spectroscopy[23]. Assuming this phase locking of two harmonics in the energy region 60-64 eV produced the attosecond pulse trains in the model simulation, and also defines the individual attosecond pulse duration to ~600 as, as stated in the Methods Summary section of the main text.

Measuring the Wave-Packet Phase in Real/Elapsed Time. In the experiment, we measured changes of the spectrally resolved absorbance (ΔOD), as a function of time delay τ between an attosecond-pulsed XUV excitation and a VIS coupling pulse. For the case of weak VIS intensity, the coupling process can be considered a weak-field probe process, which does not significantly affect the phases nor the population of the quantum states 2s2p and $sp_{2,3+}$ contributing to the wave packet

$$|\Psi(t)\rangle \propto \exp(-\Gamma_{2s2p}/2\, t)|2s2p\rangle + a \exp[-i\varphi(t)] \exp(-\Gamma_{sp23+}/2\, t)|sp_{2,3+}\rangle.$$

In the simulations shown in Extended Data Fig. 5, conducted at the same intensity as for the experimental results in Fig. 2a, we confirmed that population transfer to the near-resonant $2p^2$ state was below 10%. In that weak-field case, the measured ΔOD versus *delay* time τ can be converted into an information on the wave-packet states' relative-phase evolution $\varphi(t)$ in *real* time t (elapsed time after excitation). For the definition of elapsed/real time zero, we used the arrival time of the exciting attosecond pulse, or the most intense central attosecond pulse in the case of a short pulse train, as depicted in Extended Data Fig. 5. A lineout of ΔOD vs. delay time

at a spectral position near the $sp_{2,3+}$ resonance at 63.67 eV (where ΔOD shows pronounced changes with time delay) is shown in Extended Data Fig. 6a, and used for the mapping of ΔOD in delay to $\varphi(t)$ in real time. The oscillation of $\Delta OD(\tau)$ is almost fully independent of whether the excitation occurs with isolated attosecond pulses, or pulse trains of two or several attosecond pulses. The wave-packet phase $\varphi(t)$, defined as the time-dependent phase difference between the 2s2p and $sp_{2,3+}$ state coefficients, was read out from the simulation for all pulse configurations and compared to the phase $\varphi_{OD}(\tau)$ of the oscillation with $\Delta OD(\tau) \propto \cos[\varphi_{OD}(\tau)] + const.$ for $t = \tau$, as shown in Extended Data Fig. 6b. The phase $\varphi_{OD}(\tau)$ was retrieved via Fourier analysis, taking the full modulation bandwidth into account as shown in Extended Data Fig. 5g,h. The phases of the wave packet, as excited by the different pulse configurations, agree excellently, proving again the good definition of the wave packet even in the absence of isolated attosecond pulses or CEP locking. The difference between $\varphi_{OD}(\tau)$ (measurable quantity) and $\varphi(t)$ (the relative phase between the quantum states defining the wave packet) was extracted and is shown in Extended Data Fig. 6c. This phase difference is almost independent of the XUV excitation configuration (isolated vs. trains of attosecond pulses), and was thus used in the experiment to retrieve the wave-packet phase as a function of elapsed time t from the measured $\Delta OD(\tau)$ data. The experimental result is shown in Fig. 2d,e in the main text, where the error bar on the experimental wave-packet phase reconstruction as shown there includes the small error given by the experimental uncertainty on the exact attosecond pulse-train configuration, as discussed here. In Extended Data Fig. 6d, we also show that the amplitude ratio a of the wave packet remains well defined (within 10% amplitude-ratio fluctuations) despite the differences in the XUV excitation configurations. Fluctuations on the order of 10% in the high-harmonic spectra are typically present also in CEP-stabilized laser systems driving HHG, either by CEP noise or shot-to-shot driver-pulse intensity noise.

Line-Shape Analysis for Phase Retrieval. As was demonstrated in Ref. 13, the Fano q asymmetry parameter can be directly related to a phase shift φ of the temporal dipole response after delta-like excitation via

$$\varphi = 2\arg(q - i). \qquad (9)$$

This phase shift can be controlled using a short-pulsed laser field as described in connection to Fig. 4 in the main paper. The laser-controlled phase manipulation of the states right after excitation can thus be read out via fitting a Fano line shape to the measured absorption spectrum. The absorption line shape obtained from the *ab-initio* simulation (shown in Fig. 4b in the main paper), is directly fitted with an asymmetric Fano line profile, using

$$S_{FANO} = \frac{a}{q^2+1}\left[\frac{(q+\varepsilon)^2}{1+\varepsilon^2} - 1\right] + b \quad \text{with the reduced energy} \qquad \varepsilon = \frac{E - E_r}{\Gamma/2}, \qquad (10)$$

where all parameters such as the strength a, the offset b, the asymmetry parameter q, the resonance position E_r and the decay width Γ converged to a least squares minimum. Both the fitted intensity-dependent amplitude $a(I)$, and phase $\varphi(I)$, where the latter was obtained from q

after using Eq. (9), perfectly agree with the states' complex expansion coefficients. This is shown for the intensity-dependent phase $\varphi(I)$ of the 2s2p and $sp_{2,3+}$ states in Fig. 4e/f in the main text. Extended Data Fig. 7c,d show the related fitted line shapes for several VIS laser intensities in the energy region where the least-squares fit was performed, which is 60.11 to 60.21 eV for the 2s2p, and 63.56 to 63.76 eV for the $sp_{2,3+}$ state. Fitting the experimentally recorded line shapes, the finite spectrometer resolution was taken into account, which is on the order of the decay width of the states. Since the XUV intensity $I_{SIG}(E)$ was measured after transmission through the helium target, $10^{[-SFANO]}$ needed to be convolved with the spectrometer response function, which excluded the formulation of an analytical fit function. Formally, the experimentally observed line shape is parametrized via

$$S_{FANO,EXP} = -\mathrm{Log}_{10}\left[\left(10^{-S_{FANO}}\right)\otimes\frac{1}{\sqrt{2\pi}\sigma}\exp\left[-\frac{E^2}{2\sigma^2}\right]\right] \qquad (11)$$

where $\otimes$ denotes the convolution, S_{FANO} is given in Eq. (10), and σ = 0.020 eV is the experimentally determined detector resolution. In the presence of experimental noise and limited amount of data points both E_r and Γ were kept constant for all VIS laser intensities using literature values. $S_{FANO,EXP}$ was numerically computed in the parameter space spanned by q, a and b, and the sum of mean squares was minimized with respect to the experimental data points within the same energy region as above. The results are shown in Extended Data Fig. 7a,b and confirm the convergence of the numerically performed minimization procedure. The intensity dependent phase $\varphi(I)$, extracted from Fano line shape analysis, is shown in Fig. 4c,d in the main text. The error bar was determined by fitting three equivalent experimental data sets and computing the standard deviation.

Online Methods References

31. Argenti,L. & Moccia,R. Helium 2(3)S photoionization up to the N=5 threshold. *J. Phys. B* **41**, 035002 (2008).

32. Krausz, F. and Ivanov, M. Attosecond physics. *Rev. Mod. Phys.* **81**, 163-234 (2009).

33. Henke, B., Gullikson, E., and Davis, J. X-Ray Interactions: Photoabsorption, Scattering, Transmission, and Reflection at E = 50-30,000 eV, Z = 1-92. *At. Data and Nucl. Data Tabl.* **54**, 181-342 (1993). http://www.cxro.lbl.gov/

34. Domke, M., Schulz, K., Remmers, G., Kaindl, G. and Wintgen, D. High-resolution study of $^1P^o$ double-excitation states in helium. *Phys. Rev. A* **53**, 1424-1438 (1996).

35. Santra, R., Yakovlev, V. S. , Pfeifer, T. and Loh, Z.-H. Theory of attosecond transient absorption spectroscopy of strong-field-generated ions. *Phys. Rev. A* **83**, 033405 (2011).

36. Samson, J. A. R., He, Z. X., Yin, L. and Haddad, G. N. Precision measurements of the absolute photoionization cross-sections of He. *J. Phys. B* **27**, 887 (1994).

37. Hicks, P. J. and Comer, J. Ejected electron spectroscopy of autoionizing states excited by low energy electron impact. *J. Phys. B* **8**, 1866 (1975).

38. Bürgers, A., Wintgen, D. and Rost, J.-M. Highly doubly excited S states of the helium atom**.** *J. Phys. B* **28**, 3163-3183 (1995).

39. Lindroth, E. *private communication* (2011).

Extended Data Figure Legends

Extended Data Figure 1 | Experimental Apparatus & Recorded Data. a, Design view of the experimental setup, consisting of a neon (Ne) gas target for high-harmonic generation (HHG), a motorized iris aperture, a split mirror (SM) in combination with a thin silicon nitride (Si_3N_4) membrane and an aluminium (Al) filter, a focusing toroidal mirror (TM), a dense (~100 mbar) absorbing helium (He) target, and a home-built high-resolution spectrometer, which consists of a variable line spacing (VLS) grating, a cooled (−50 °C) XUV CCD camera, and a pair of Al filters for stray-light suppression. **b**, Recorded XUV reference spectra (no He gas in target cell, black line) in the 50 to 70 eV energy range, averaged over ~64,000 laser shots, and recorded XUV signal spectra after transmission through the dense He gas target (red line), averaged over ~640,000 laser shots. The statistical error is on the order of the line thickness. **c**, Two-dimensional absorbance at a calibrated VIS peak intensity of 3.3×10^{12} W/cm^2. The plot consist of 300 single absorbance spectra (details and definition see Methods, section "Experimental Data Acquisition"), that were obtained with a time-delay step size of ~170 as.

Extended Data Figure 2 | Few-Level Model Simulation Details. a, Level scheme of the simulated sub-system, including the ground state $|g\rangle \equiv |1s^2\rangle$, the autoionizing bound states $|a\rangle \equiv |2s2p\rangle$, $|b\rangle \equiv |2p^2\rangle$ and $|c\rangle \equiv |sp_{2,3+}\rangle$, and the continua $|1s,\varepsilon p\rangle$ and $|1s,\varepsilon s\rangle$, all coupled via the dipole matrix elements d_{nm} as depicted. The configuration-interaction matrix elements $V_{\varepsilon,n}$ couple the excited states with their corresponding (symmetry $^1P^o$ or $^1S^e$) continua. **b**, Schrödinger equation describing the temporal evolution of the coupled states' expansion coefficients $c_n(t)$, resulting from the respective coupling pathways as depicted in (**a**). Further explanations and definitions of parameters are given in Methods, section "Few-Level Model Simulation". **c**, Simulated 2D absorbance plot of the few-level system assuming a quasi-monochromatic VIS field of 730 nm wavelength. The absorbance spectra were temporally averaged over one VIS laser cycle (XUV/VIS delay), and convoluted with the experimental detector resolution (σ = 20 meV). **d**,**e**,**f**, Simulated temporal evolution of $|c_n(t)|$ of the three autoionizing states 2s2p ($^1P^o$; black lines), $2p^2$ ($^1S^e$; blue lines), and $sp_{2,3+}$ ($^1P^o$; red lines) where the $^1P^o$-symmetry states were weakly populated by an XUV attosecond pulse at time t = 0 fs. All states were coupled by the VIS field (7 fs, 730 nm, 3×10^{12} W/cm^2) at three different time delays τ. The dashed curves show the states' evolution in absence of the VIS field.

Extended Data Figure 3 | Intensity calibration of the experimental data. a, Calculated absorbance for a 7 fs, ~730 nm VIS laser pulse at increasing intensity. **b**, Experimentally measured absorbance for increasing openings of the iris diaphragm. For **a** and **b**, the time delay was set to where the Autler–Townes splitting is at maximum, averaged over two modulation periods. **c**, The comparison of maximum absorbance of the left-shifting 2s2p line (starting from 60.15 eV) between numerical and experimental results yields an *in-situ* mapping between the

VIS intensity and the iris opening in the experiment (black line). The grey shaded area denotes the standard deviation, taking into account different VIS durations and an additional comparison near 0 fs time delay, and forms a systematic uncertainty of the monotonically increasing intensity-calibration curve.

Extended Data Figure 4 | Effects of the Attosecond Pulse Configuration and the Carrier Envelope Phase. a, Simulated absorbance plots (**top row**) for different XUV pulse configurations: Two attosecond pulses, $\varphi_{CEP} = \pi/2$ (**left**); One attosecond pulse, $\varphi_{CEP} = 0$ (**middle**); One attosecond pulse, $\varphi_{CEP} = \pi/2$ (**right**). The VIS pulse duration was 7 fs with 3×10^{12} W/cm^2 peak intensity, where the respective XUV/VIS pulse configurations are illustrated at zero time delay (**bottom row**). **b**, Experimentally measured absorbance plots for stabilized (**top left**), with residual CEP noise 0.38 rad, root-mean-square, and non-stabilized (**top right**) CEP. The observed time-dependent features, including the lineout at photon energy 63.66 eV (**bottom**) are practically identical for the CEP- vs. the non-CEP-stabilized measurement. Any significant temporal jitter between the attosecond pulses and the VIS carrier wave in the HHG process, for the case of statistical CEP, would approximately correspond to an averaging over a range of time delays for the case of a CEP-stable measurement, smearing out sub-cycle oscillations in the absorbance. This is clearly not observed.

Extended Data Figure 5 | Simulated absorbance changes (ΔOD) for low VIS intensity and different pulse configurations. a, One attosecond pulse, $\varphi_{CEP} = 0$. **b**, One attosecond pulse, $\varphi_{CEP} = \pi/2$. **c**, Two attosecond pulses, $\varphi_{CEP} = 0$. **d**, Two attosecond pulses, $\varphi_{CEP} = \pi/2$. **e**, Multiple attosecond pulses (pulse train), $\varphi_{CEP} = 0$. **f**, Multiple attosecond pulses (pulse train), $\varphi_{CEP} = \pi/2$. The **lower panels** show the respective pulse configuration at zero time delay. The VIS pulse duration was 7 fs and the intensity was 3×10^{10} W/cm^2. **g**,**h**, Power spectral density distribution of the ΔOD oscillation of the experiment (**g**) and the simulation (**h**). The frequency range employed in the analysis is marked in red. Via filtering from near zero frequency up to the Nyquist frequency, we used the full modulation bandwidth to retrieve the phase $\varphi_{OD}(\tau)$.

Extended Data Figure 6 | Reconstruction of the wave packet from time-delay dependent ΔOD(τ) data near the $sp_{2,3+}$ resonance at 63.67 eV, simulation results. a, ΔOD(τ) for the different excitation scenarios shown in Extended Data Fig. 5. **b**, The phase $\varphi_{OD}(\tau)$ extracted from the ΔOD(τ) oscillations (solid lines), compared to the phase $\varphi(t)$ of the wave packet (dashed lines) for the different excitation configurations. **c,** The difference between the (measurable) modulation phase $\varphi_{OD}(\tau)$ and the wave-packet phase $\varphi(t)$ for each of the excitation scenarios. A time-delay dependent correction phase of ~0.4π rad needs to be taken into account to reconstruct the wave-packet phase $\varphi(t)$ in the experiment from the measured ΔOD(τ), as shown in Fig. 2 of the main text. **d**, The variation of the wave-packet amplitude ratio for the different excitation configurations. Even in the extreme case of multiple attosecond pulses, the amplitude ratio is well defined within a region of ±10%.

Extended Data Figure 7 | Fitting the intensity-dependent spectral line shapes of the 2s2p and the $sp_{2,3+}$ resonances. a,**b**, Least squares fit to the experimentally measured line shape as shown in Fig. 4a in the main text. The laser-controlled line shape is shown for several laser intensities as given in the figure. **c**,**d**, Least squares fit to the theoretically predicted line shape obtained from the *ab-initio* simulation as shown in Fig. 4b in the main text, also for several laser

intensities as denoted in the figure. For all cases, the restricted energy region of the least squares fit [2s2p: 60.11 to 60.21 eV (**a**,**c**); $sp_{2,3+}$: 63.56 to 63.76 eV (**b**,**d**)] ensures phase retrieval for times after the interaction with the laser pulse.

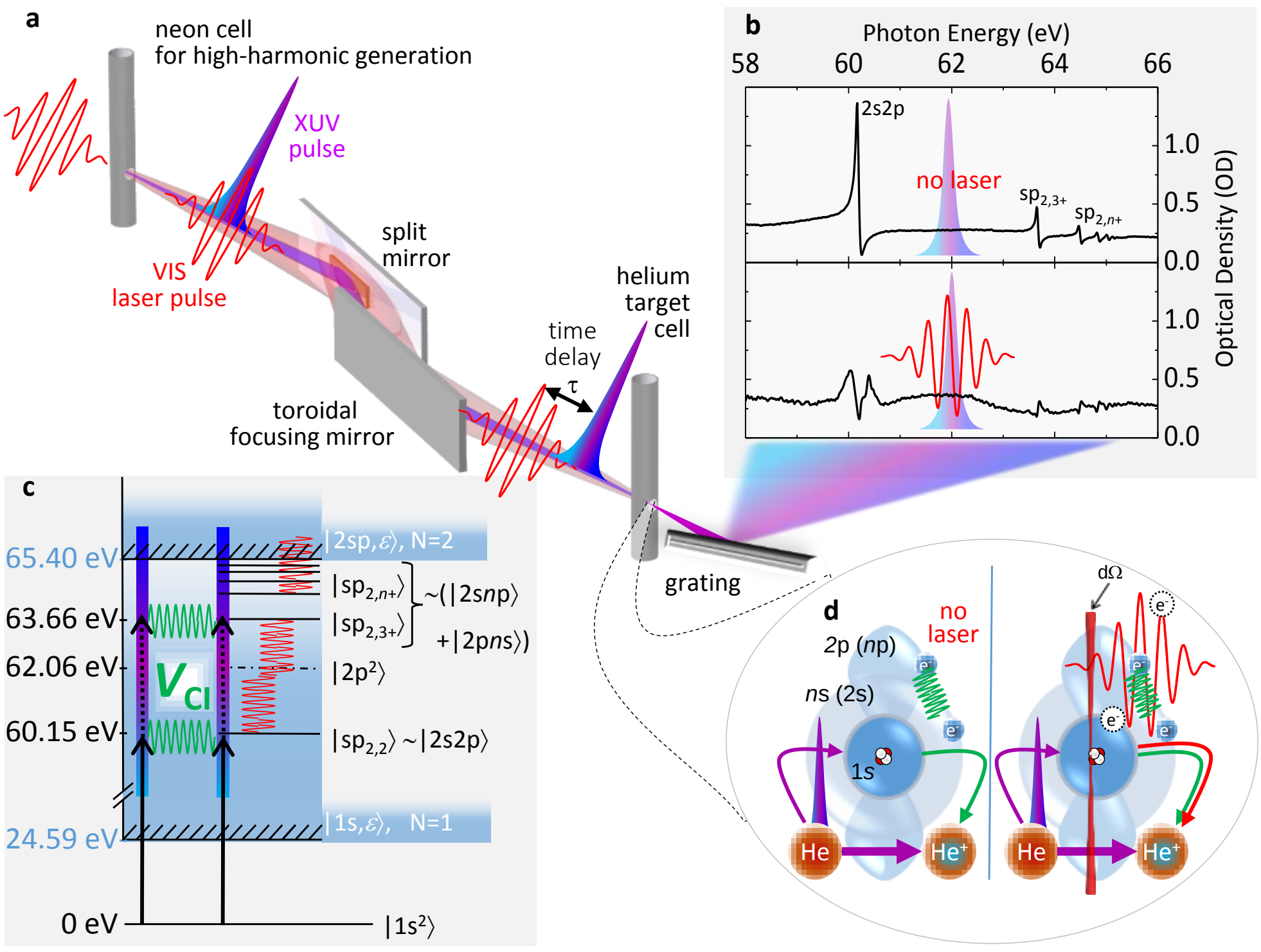
a
neon cell
for high-harmonic generation
XUV
pulse
VIS
laser pulse
split
mirror
toroidal
focusing mirror
time
delay
τ
helium
target
cell
grating
b
Photon Energy (eV)
58
60
62
64
66
2s2p
no laser
sp2,3+
sp2,n+
1.0
0.5
0.0
1.0
0.5
0.0
Optical Density (OD)
c
65.40 eV
63.66 eV
62.06 eV
60.15 eV
24.59 eV
0 eV
|2sp,ε⟩, N=2
|sp2,n+⟩
|sp2,3+⟩
~(|2snp⟩
+|2pns⟩)
|2p²⟩
|sp2,2⟩ ~|2s2p⟩
|1s,ε⟩, N=1
|1s²⟩
VCI
d
no
laser
2p (np)
ns (2s)
1s
He
He+
dΩ
e-

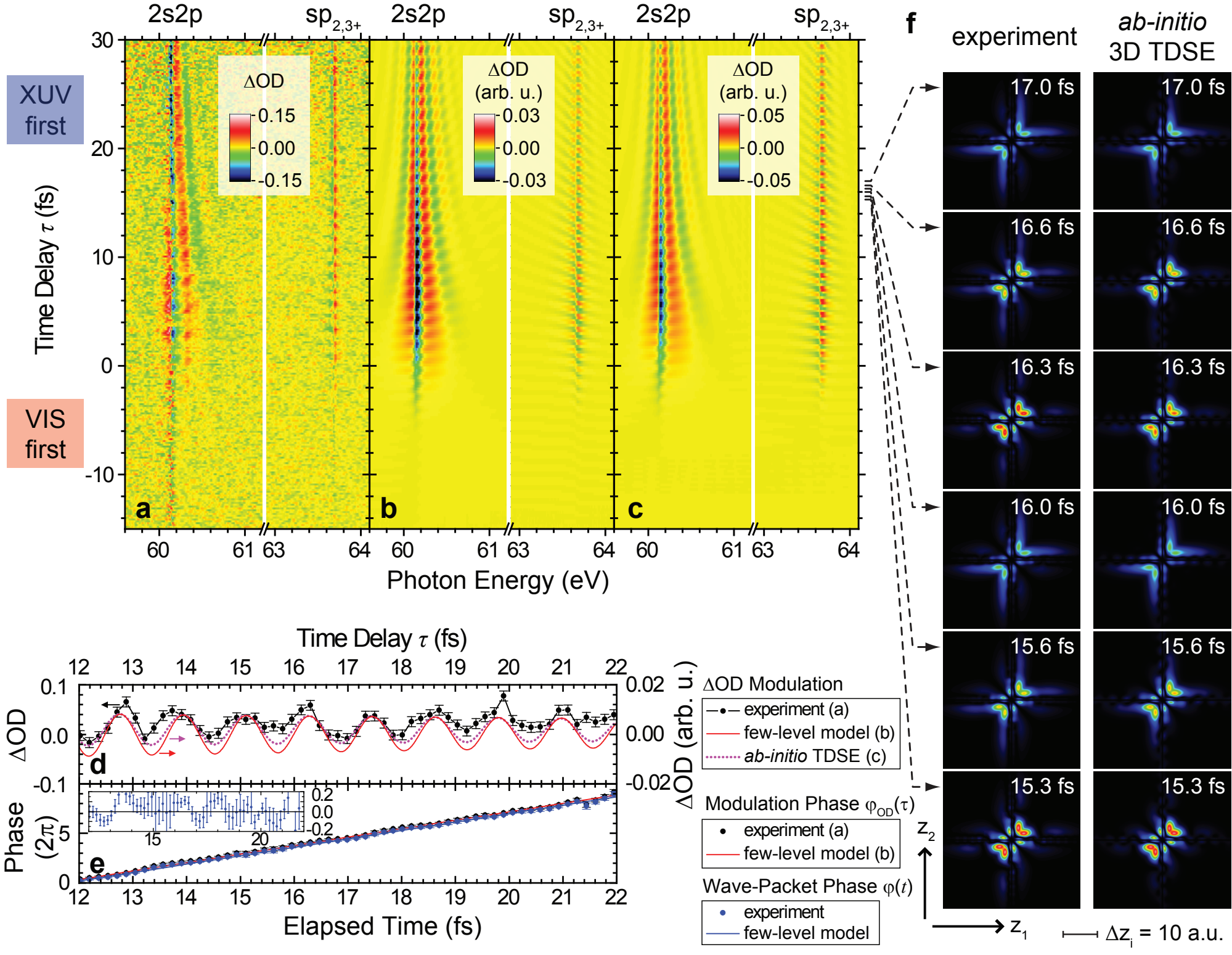
2s2p
sp2,3+
XUV first
VIS first
Time Delay τ (fs)
ΔOD
0.15
0.00
-0.15
ΔOD (arb. u.)
0.03
0.00
-0.03
ΔOD (arb. u.)
0.05
0.00
-0.05
a
b
c
Photon Energy (eV)
f
experiment
ab-initio 3D TDSE
17.0 fs
16.6 fs
16.3 fs
16.0 fs
15.6 fs
15.3 fs
Time Delay τ (fs)
ΔOD
d
Phase (2π)
e
Elapsed Time (fs)
ΔOD (arb. u.)
ΔOD Modulation
experiment (a)
few-level model (b)
ab-initio TDSE (c)
Modulation Phase φOD(τ)
experiment (a)
few-level model (b)
Wave-Packet Phase φ(t)
experiment
few-level model
z2
z1
Δzi = 10 a.u.

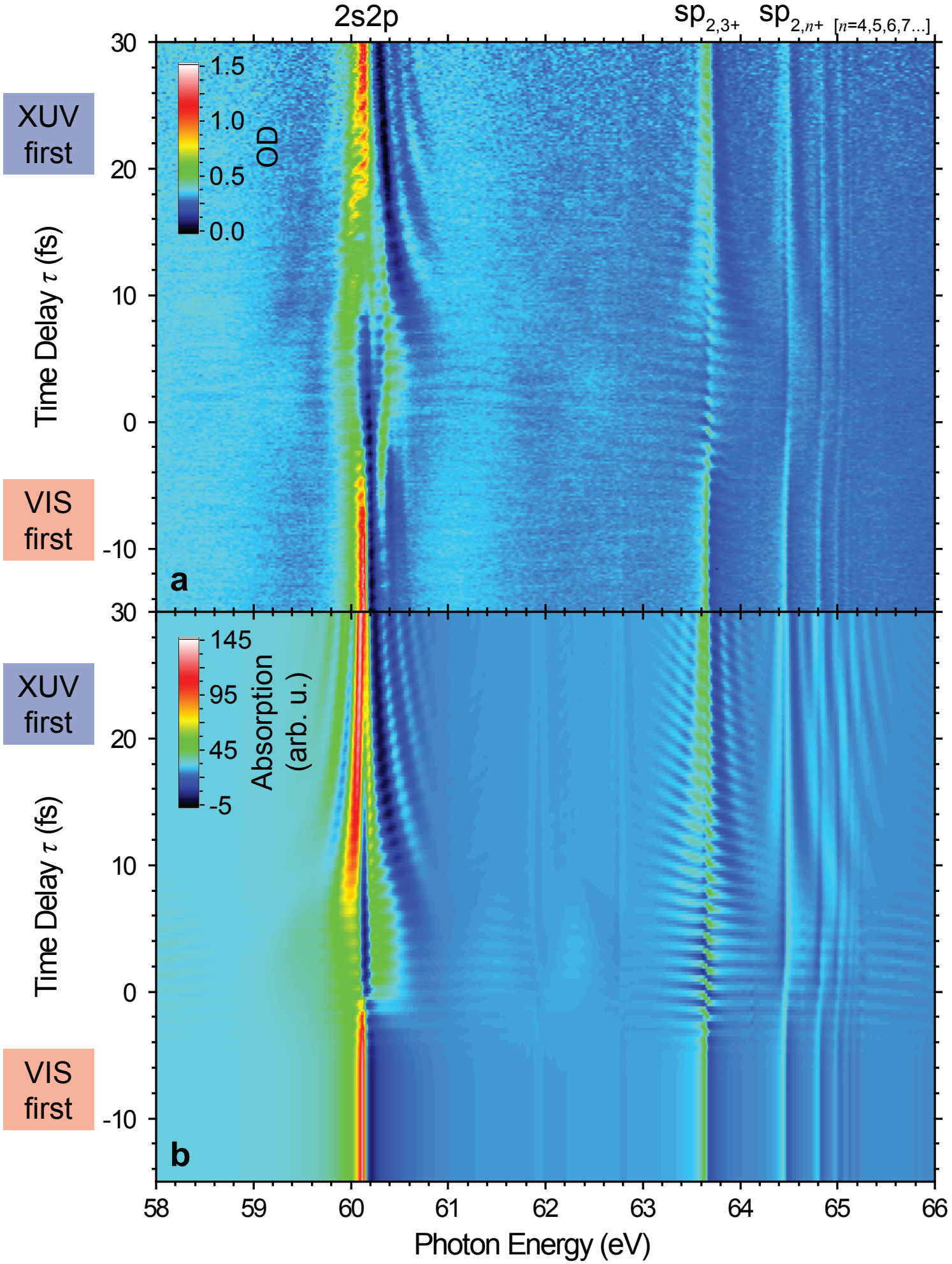
2s2p
sp2,3+
sp2,n+ [n=4,5,6,7...]
XUV first
VIS first
Time Delay τ (fs)
30
20
10
0
-10
1.5
1.0
0.5
0.0
OD
a
145
95
45
-5
Absorption (arb. u.)
b
58
59
60
61
62
63
64
65
66
Photon Energy (eV)

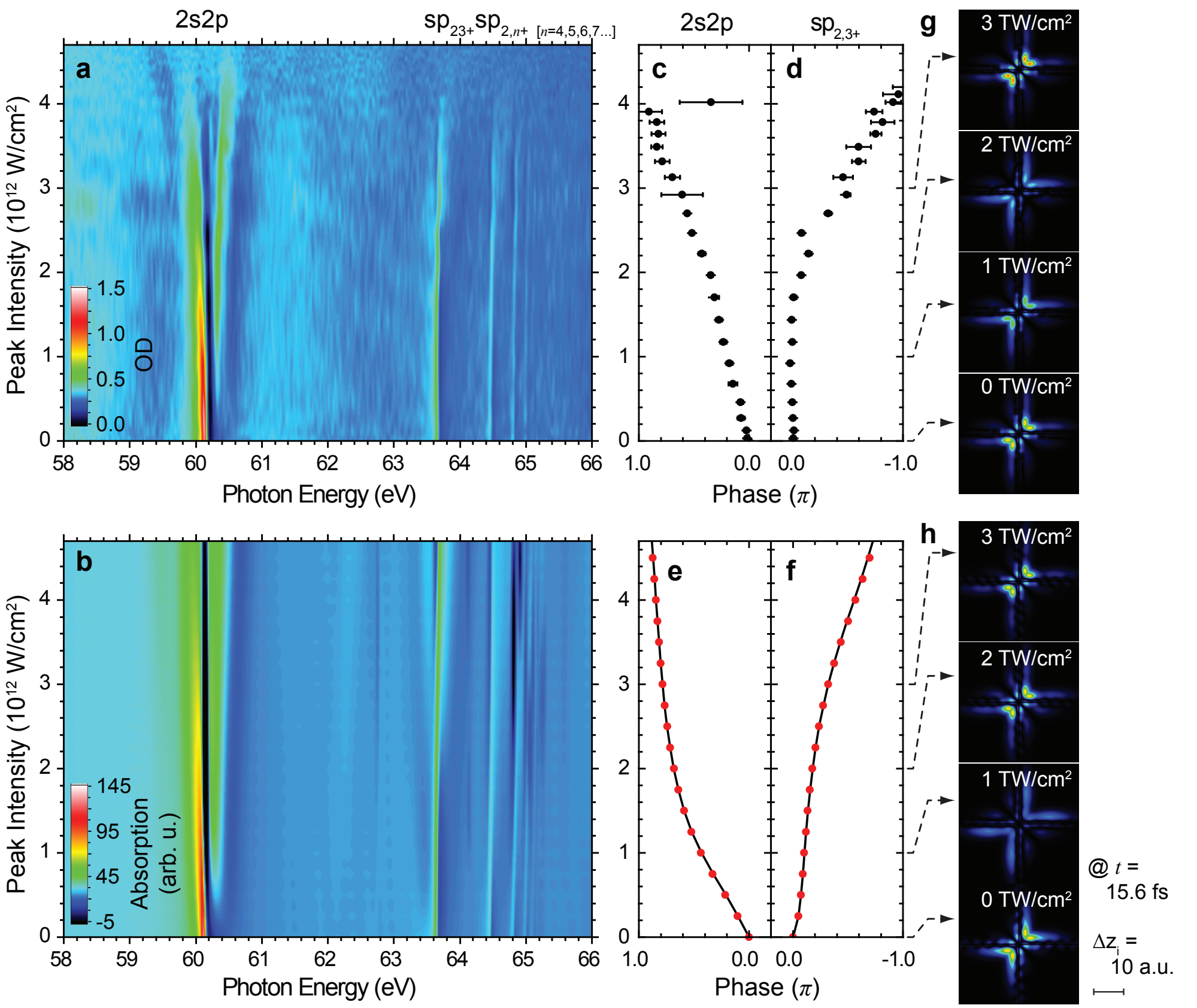
2s2p
sp23+sp2,n+ [n=4,5,6,7...]
a
b
c
d
e
f
g
h
Peak Intensity (10^12 W/cm^2)
Photon Energy (eV)
OD
Absorption (arb. u.)
2s2p
sp2,3+
Phase (π)
3 TW/cm^2
2 TW/cm^2
1 TW/cm^2
0 TW/cm^2
@ t = 15.6 fs
Δz_i = 10 a.u.